Global 1km Land Surface Parameters for Kilometer-Scale Earth System Modeling

Lingcheng Li, Gautam Bisht, Dalei Hao, L. Ruby Leung

Atmospheric Sciences and Global Change Division, Pacific Northwest National Laboratory, Richland, WA, USA

@LingchengL; @GBISHT80; @DaleiHao

Correspondence: Lingcheng Li (lingcheng.li@pnnl.gov)

This manuscript is currently available as a preprint on EarthArXiv and has been submitted to the Earth System Science Data journal for peer review. Please note that subsequent versions of this manuscript may contain revisions and updates. Please feel free to contact us with any feedback, discussion, or comments from the scientific community. Your input is greatly appreciated.

Abstract

Earth system models (ESMs) are progressively advancing towards the kilometer scale (k-scale). However, the surface parameters for Land Surface Models (LSMs) within ESMs running at the k-scale are typically derived from coarse resolution and outdated datasets. This study aims to develop a new set of global land surface parameters with a resolution of 1 km for multiple years from 2001 to 2020, utilizing the latest and most accurate available datasets. Specifically, the datasets consist of parameters related to land use and land cover, vegetation, soil, and topography. To demonstrate the capability of these new parameters, we conducted 1 km resolution simulations using the E3SM Land Model version 2 (ELM2) over the contiguous United States. Our results demonstrate that land surface parameters contribute to significant spatial heterogeneity in ELM2 simulations of soil moisture, latent heat, emitted longwave radiation, and absorbed shortwave radiation. On average, about 31% to 54% of spatial information is lost by upscaling the 1 km ELM2 simulations to a 12 km resolution. Using eXplainable Machine Learning (XML) methods, the influential factors driving the spatial variability and spatial information loss of ELM2 simulations were identified, highlighting the substantial impact of the spatial variability and information loss of various land surface parameters, as well as the mean climate conditions. The new land surface parameters are tailored to meet the emerging needs of k-scale LSMs and ESMs modeling with significant implications for advancing our understanding of water, carbon, and energy cycles under global change. The 1 km land surface parameters are publicly available at https://doi.org/10.25584/PNNLDH/1986308 (Li et al., 2023).

1. Introduction

Aided by advancements in computing power, it has become increasingly feasible to run land surface models (LSMs) and Earth system models (ESMs) at the kilometer scale (k-scale) to improve our understanding of Earth system processes. The emergence of k-scale modeling has the potential to improve the accuracy of climate simulations significantly and allow for explicit modeling of physical processes that were previously poorly represented in climate models (Nat. Clim. Chang. 2022), such as modeling of mesoscale convective systems in the atmosphere (Slingo et al., 2022) and mesoscale eddies in ocean (Hewitt et al., 2022). Simultaneously, land modeling has also witnessed a surge of interest in hyper-resolution modeling, initially proposed by Wood et al. (2011), which aims to model land surface processes at a horizontal resolution of 1 km globally and 100 m or finer for continental or regional domains. The motivation behind hyper-resolution modeling is to address the requirements of operational forecasting like extreme events, and to enhance our understanding of hydrological and biogeochemical cycling, and land–atmosphere interactions. High-resolution LSMs have been increasingly applied in various fields, as demonstrated by recent examples, such as 30-meter soil moisture simulations over the contiguous United States (CONUS) (Vergopolan et al., 2020, 2021, 2022), 500-meter hyper-resolution modeling of surface and root zone soil moisture over Oklahoma (Rouf et al., 2021), 1-km simulations over Southwestern US (Singh et al., 2015), 3-km simulations over eastern Tibetan Plateau to understand hydrological changes over mountainous regions (Yuan et al., 2018; Ji and Yuan, 2018), 6-km simulations over China to reduce simulations errors of hydrological variables (Ji et al., 2023). High-resolution modeling can better capture the land surface heterogeneity and could improve simulations of terrestrial water, energy, and biogeochemical cycles, as well as land and atmosphere coupling (Giorgi and Avissar, 1997; Chaney et al., 2018; Zhou et al., 2019; Liu et

al., 2017; Bou-Zeid et al., 2020; Chen et al., 2020; Nitta et al., 2020; Vrese et al., 2016). Singh et al. (2015) demonstrated that increasingly capturing topography and soil texture heterogeneity at finer resolutions (e.g., 1 km) improves land surface modeling of water and energy variables. Li et al. (2022) have shown that the spatial heterogeneities of land surface parameters (including land use and land cover (LULC) and topography) are essential for modeling the spatial variability of land surface energy and water partitioning. Hao et al. (2022) found that 1 km simulations with sub-grid topographic configurations can better capture the topographic effects on surface fluxes.

The parameters for LSMs within ESMs being run at the k-scale are typically derived from coarse resolution datasets or outdated datasets. Consequently, k-scale modeling may not accurately represent fine-scale land surface heterogeneity unless high-resolution land surface parameters at the kilometer or finer scales are utilized. Publicly available land surface parameters are primarily provided at coarse resolutions and based on outdated datasets. For example, the Community Land Model version 5 (CLM5; Lawrence et al., 2019) typically relies on land surface parameters with spatial resolutions ranging from 1km to 0.5º based on source datasets that were processed more than 10 years ago (see Table 1 for details). Although LULC-related parameters are available at a relatively high resolution of 0.05º, they are temporally static and were derived from a combination of data from different years spanning 1993 to 2012 (Table 1). Leaf area index (LAI) was derived from the now outdated products of Moderate Resolution Imaging Spectroradiometer (MODIS) collection 4 (Myneni et al., 2002). The canopy height for tree Plant Functional Types (PFTs) is based on forest canopy height data derived from the Geoscience Laser Altimeter System (GLAS) aboard ICESat, collected in 2005 (Simard et al., 2011). Canopy height for short vegetation is represented by PFT-specific values that remain invariant in space (Bonan et

al., 2002). Soil sand and clay content were obtained from the International Geosphere-Biosphere Programme (IGBP) soil dataset (Global Soil Data Task 2000) consisting of 4931 soil mapping units (IGBP, 2000). These CLM5 land surface parameters have been widely utilized in the LSMs and ESMs community, despite being developed over a decade ago. Subsequently, Ke et al. (2012; hereafter referred to as K2012) developed an updated set of LULC and vegetation-related land surface parameters for CLM4 at a resolution of 0.05º. These parameters were developed based on MODIS collection 5 products or datasets derived from MODIS collection 5 products, including PFTs and non-vegetation land cover, LAI, and Stem Area Index (SAI). K2012 has also been widely used by LSMs, including CLM (e.g., Leng et al., 2013; Singh et al., 2015; Ke et al., 2013; Xia et al., 2017) and the Energy Exascale Earth System Model (E3SM) Land Model (ELM) (e.g., Caldwell et al., 2019; Leung et al., 2020; Li et al., 2022). However, the CLM5 and K2012 datasets, with their relatively coarse resolution and reliance on outdated data from over a decade ago, may not fully meet the requirements for k-scale modeling. Additionally, these datasets include LULC, LAI, and SAI that are year invariant. Consequently, they are inappropriate for studies involving LULC changes, such as urbanization. In addition, some recently developed land surface processes and their associated parameters are not included in previous datasets. For instance, Hao et al. (2021) introduced a sub-grid topographic parameterization of solar radiation with five associated topographic factors in ELM, which have been found to significantly affect the surface energy budget.

High-resolution and up-to-date datasets at kilometer or finer resolutions are now widely available and can be utilized to derive more accurate land surface parameters for k-scale LSM simulations. For example, the MODIS Land Cover Type Collection 6 (MCD12Q1 C6) data

product provides global land cover types yearly from 2001 to the present (Friedl et al., 2019; Sulla-Menashe et al., 2019) at 500-meter resolution. Compared to the MODIS Collection 4 (used in CLM5 land surface parameters) and Collection 5 products (used in K2012 land surface parameters), the C6 data represents a significant advancement in algorithm improvements and the quality of land cover information. Despite the availability of high-resolution MODIS LAI products, such as the 500 m MCD15A2H (Myneni et al., 2021), they suffer from noise and gaps with spatially and temporally inconsistent values due to clouds, seasonal snow cover, instrument issues, and uncertainties in retrieval algorithms (Yuan et al., 2011). To address these limitations, Yuan et al. (2011) reprocessed MODIS LAI products and generated a more accurate and spatiotemporally continuous and consistent LAI dataset that is available continuously to the present period. Additional high-resolution and up-to-date datasets are available for preparing land surface parameters, such as soil texture and soil organic matter at 250-meter resolution (Poggio et al., 2021) and vegetation height at 10-m resolution (Lang et al., 2022).

This study aims to develop a new set of global land surface parameters with a resolution of 1 km for multiple years, utilizing the latest and most accurate available datasets. These parameters will be tailored to meet the needs of k-scale Earth system modeling. The newly developed land surface parameters include four categories: (1) LULC-related parameters, such as the spatial distributions of PFTs, lakes, wetlands, urban areas, and glaciers; (2) vegetation-related parameters, including PFTs' LAI and SAI for multiple years ranging from 2001 to 2021, and the canopy top and bottom height; (3) soil-related parameters, such as soil textures and soil organic matter; and (4) topography-related parameters, such as slope, aspect, and sub-grid topographic factors. We employed the ELM version 2 (ELM2) as a testbed to demonstrate the capability of the

new high-resolution parameters by conducting a 5-year 1 km resolution simulation over the CONUS. We performed a spatial scaling analysis on four ELM2 simulated variables, which included soil moisture, latent heat, emitted longwave radiation, and absorbed shortwave radiation, to underscore the significance of high-resolution land surface parameters on ELM2 simulations. We employed eXplainable Machine Learning (XML) methods to evaluate the most important factors of land surface parameters and climate conditions (e.g., mean temperature and precipitation) in driving the spatial variability and spatial information loss of ELM2 simulations.

2. Development of 1km land surface parameters

In this study, all the land surface parameters were developed globally at a resolution of approximately 1 km (i.e., 1/120°, hereafter referred to as 1 km; Table 1). The LULC-related parameters, soil properties, canopy height, and elevation were processed via Google Earth Engine (GEE; Gorelick et al., 2017). The LAI was processed using an area-weighted average from its original 450 m resolution obtained from Beijing Normal University (Yuan et al., 2011). The detailed methods for deriving these parameters are described below.

Table 1 Comparison between new and previous land surface parameters

Category	Land surface parameters	This study	ELM2 / CLM5 *	K2012
LULC	PFTs, Lake, Glacier, Urban	• Resolution: 1 km, yearly, 2001-2020 • Data source: 500 m, yearly, MODIS collection 6 (Friedl et al., 2022)	• Resolution: 0.05°, temporally static, processed based on data from mixed years • PFTs data source: mixed years from 1993 to 2001; 500 m, MODIS Vegetation Continuous Fields (Hansen et al., 2003); 1 km, tree cover (Defries et al., 2000); 10 km (5 arc minutes), cropland (Ramankutty and Foley, 1999); 1 km, MODIS land cover collection 4 (Friedl et al., 2002) • Lake data source: 3 km (90 arc seconds) lake data (Kourzeneva 2009, 2010) • Glacier data source: glacier and ice sheet vector data (Arendt et al. 2012; Rastner et al. 2012) • Urban data source: 1 km urban data (Jackson et al., 2010)	• Resolution: 0.05°, year 2005 • Data source: 500 m, yearly, MODIS collection 5 (Friedl et al., 2010)
Vegetation	LAI, SAI	• Resolution: 1 km, monthly, 2001-2020 • Data source: 450 m, 8-day, reprocessed MODIS collection 6 LAI (Yuan et al., 2011; Friedl et al., 2022)	• Resolution: 0.5°, 12 months • Data source: 1 km, 8-day, MODIS collection 4 LAI (Myneni et al., 2002)	• Resolution: 0.05°, year 2005 • Data source: 450 m, 8-day, reprocessed MODIS collection 5 LAI (Yuan et al., 2011; Friedl et al., 2010)
	Canopy top height, Canopy bottom height	• Resolution: 1 km, temporally static • Data source: 10 m, vegetation canopy height (Lang et al., 2022)	• Resolution: 0.5° or PFT specified value, temporally static • Tree PFT data source: 1 km, forest canopy height derived using 2005 GLAS aboard ICESat data (Simard et al., 2011); • Short vegetation data source: PFT specific values (Bonan et al., 2002)	--
Soil	Percent sand, Percent clay	• Resolution: 1 km, temporally static • Data source: 250 m, Soilgrid v2 (Poggio et al., 2021)	• Resolution: 10 km (0.083°), temporally static • Data source: IGBP soil data of 4931 mapping units (IGBP, 2000)	--
	Soil organic matter			
Topography	Elevation	• Resolution: 1 km, temporally static • Data source: 90 m, MERIT Hydro elevation (Yamazaki et al., 2019)	• Resolution: 1 km, temporally static • Data source: USGS HYDRO1k (Verdin and Greenlee 1996)	--
	Slope			
	Standard deviation of elevation	• Resolution: 1 km, temporally static • Data source: 90 m, Hydro elevation (Yamazaki et al., 2019)	--	
	Aspect			
	Sky view factor			
	Terrain view factor			

* ELM2 and CLM5 share the same default land surface parameters, detailed descriptions available at: https://escomp.github.io/ctsm-docs/versions/release-clm5.0/html/tech_note/index.html.

2.1 LULC-related parameters

This study utilized MODIS MCD12Q1 version 6 (Friedl et al., 2022) to derive the PFT and other non-vegetation land types at a resolution of 1 km for 2001–2020. The original MODIS land cover data was first resampled to 1 km from its original 500 m resolution using a majority resampling method in GEE. At such a high 1km resolution, we did not consider the proportion of different land cover types within each grid. Instead, we assigned 100% of a grid cell to the major land cover type. Specifically, the MCD12Q1 LC_Type 5 PFT classification layer was used to determine the distributions of the seven PFTs, as well as lake, urban, and glacier, following the method outlined in Ke et al. (2012) and summarized below:

- The seven PFTs include needleleaf evergreen trees (NET), needleleaf deciduous trees (NDT), broadleaf evergreen trees (BET), broadleaf deciduous trees (BDT), shrub (SHR), grass (GRS), and crop (CRO). These PFTs were further reclassified into 15 categories (Table S1) that are typically used in LSMs based on the rules presented in Bonan et al. (2002a) with the assistance of 1 km precipitation and surface air temperature from WorldClim V1 (Hijmans et al., 2005).
- Grass was reclassified as C3 and C4 grass using the approach presented by Still et al. (2003), with the assistance of monthly LAI (processed in section 2.2.1) and meteorological variables from WorldClim V1.
- The "non-vegetated land" was classified as barren soil class.
- The "permanent snow and ice" was assigned as the glacier land unit. Global lakes were identified based on the classification of "water bodies" over the global land, constrained using the global land mask obtained from Natural Earth (https://www.naturalearthdata.com/).

- The urban land unit was determined based on the MODIS "urban and built-up" classification. These urban grids were further classified into three urban classes, namely, tall building district (TBD), high density (HD), and medium density (MD), based on Jackson et al. (2010; hereinafter referred to as J2010). J2010 generated global urban extent maps for the TBD, HD, and MD classes at a spatial resolution of 1 km, based on rules of building height and vegetation coverage fraction (https://gdex.ucar.edu/dataset/188a_oleson/file.html). However, the J2010 dataset is temporally static and cannot reflect changes in urban boundaries over time. Therefore, we reclassified the yearly MODIS urban land class as TBD, HD, and MD based on the J2010 dataset using the nearest neighbor sampling method for each year.

After determining the distribution of 15 PFTs, bare soil, lake, glacier, and urban land, any remaining 1 km grids were assigned as ocean (Table S1). It should be noted that the wetland land unit was not explicitly classified in this study. This is because, instead of treating wetlands as an individual land unit, many LSMs (e.g., ELM2 and CLM5) integrate wetland functioning processes prognostically within other land units where a surface water storage component is implemented to represent wetland functioning.

2.2 Vegetation-related parameters

2.2.1 Monthly LAI and SAI

The monthly LAI parameters were obtained from Beijing Normal University (BNU_LAI; Yuan et al., 2011). BNU_LAI is a reprocessed version of the MODIS LAI C6 product, which has undergone comprehensive quality control and use of multiple algorithms (Yuan et al., 2011). The data have better performance in validation against reference LAI and are more spatiotemporally

continuous and consistent than the original MODIS LAI (Yuan et al., 2011). The 8-day BNU_LAI product at a resolution of 15 seconds (~450 m) over 2001–2020 was downloaded from http://globalchange.bnu.edu.cn/research/laiv061. Subsequently, the data were resampled to a resolution of 1 km using an area-weighted average method and averaged temporally for each month. The processed monthly LAI at 1 km resolution was subsequently assigned to each of the 15 PFTs described above at each grid. The monthly SAI was then calculated based on the processed monthly LAI using the methods and PFT parameters described in Zeng et al. (2002).

2.2.2 Vegetation canopy height

The global vegetation canopy height dataset used in this study was obtained from Lang et al. (2022). Lang et al. (2022) developed a probabilistic deep learning model to retrieve canopy height from the Sentinel-2 images by fusing Global Ecosystem Dynamics Investigation (GEDI). This dataset is the first globally consistent and wall-to-wall canopy height at a 10 m spatial resolution and includes canopy height for all vegetation types. The canopy height served as the canopy top height parameter. Canopy bottom height was calculated by multiplying PFT-based ratios derived from the ratio of ELM's (same as CLM5) canopy top and bottom heights for different PFTs (Table S2).

2.3 Soil-related parameters

We obtained the Soilgrid v2 data with an original resolution of 250 m (Poggio et al., 2021) to prepare soil properties. Soilgrid is generated using machine learning based on multiple data sources of soil profiles and remote sensing data (Hengl et al., 2017). Soilgrid v2 provides percent clay, percent sand, and soil organic matter for six soil layers: 0–5 cm, 5–15 cm, 15–30 cm, 30–60 cm, 60–100 cm, and 100–200 cm. The original SoilGrid version 2 data obtained from GEE were

processed at 1 km resolution with multiple layers using an area-weighted average method. To facilitate the demonstration, we restructured the six soil layers vertically into ELM's ten effective soil layers (0–1.8 cm, 1.8–4.5 cm, 4.5–9.1 cm, 9.1–16.6 cm, 16.6–28.9 cm, 28.9–49.3 cm, 49.3–82.9 cm, 82.9–138.3 cm, 138.3–229.6 cm, and 229.6–380.2 cm) using the nearest neighboring method. It should be noted that the lake module in ELM2 and CLM5 requires soil properties, but the Soilgrid v2 data may not provide coverage over water surfaces. To address this, we utilized the nearest neighbor sampling method to map the 1 km soil properties onto the terrestrial water surface.

2.4 Topography-related parameters

The 90 m digital elevation from MERIT Hydro (Yamazaki et al., 2019) was used to derive topography-related parameters. We first acquired the 1km elevation and standard deviation of elevation using GEE based on the original 90 m elevation. Further, we calculated the slope, aspect, sky view factor, and terrain configuration factor from the 1km elevation using the parallel computing tool developed by Dozier (2022). The sky view factor represents the proportion of visible sky limited by adjacent terrain, and the terrain configuration factor describes the proportion of adjacent terrain which is visible to the ground target. Finally, to drive the parameterization of sub-grid topographical effects on solar radiation (Hao et al., 2022) in ELM2, we calculated the $\sin(slope) \cdot \sin(aspect)$ and $\sin(slope) \cdot \cos(aspect)$ for calculating the local solar incident angle, and two normalized angle-related factors, the sky view factor, and terrain configuration factor by $\cos(slope)$.

3. K-scale demonstration simulation over CONUS

3.1 Experiment design

To demonstrate the capability of 1 km datasets, we conducted ELM2 simulations over CONUS at the resolution of 1 km, using the newly developed 1 km land surface parameters for 2010. We used atmospheric forcing from the Global Soil Wetness Project Phase 3 (GSWP3; Kim, 2017) with a spatial resolution of 0.5º to drive ELM. The spatial homogeneity of atmospheric forcing within 0.5º grid cell guarantees that the spatial variability of ELM simulated variables (e.g., latent heat) within 0.5º grid cell is solely attributable to the heterogeneity of the 1 km land surface parameters. There are approximately 12 million effective grids over CONUS. We ran ELM for five years (2010–2014), and the last year's simulation was used for analysis. We specifically analyzed the annual mean of surface layer soil moisture (SM, m^3/m^3), latent heat (LH, W/m^2), emitted longwave radiation (ELR, W/m^2), and absorbed shortwave radiation (ASR, W/m^2).

3.2 Spatial scaling analysis

We conducted a spatial scaling analysis following the method described in Vergopolan (2022) on the 1 km ELM simulation data to better understand how k-scale spatial heterogeneity in the four ELM-simulated variables (mentioned in Section 3.1) induced only by spatial heterogeneity of land surface parameters changes across spatial scales. First, we performed upscaling by averaging the 1 km (=1/120°) land surface parameters and the four ELM-simulated variables to coarser spatial scales, λ_{scale} of 1/60°, 1/40°, 1/30°, 1/24°, 1/20°, and 1/10°, and calculated the spatial standard deviation (σ_{scale}) within each 0.5° × 0.5° box at each spatial scale (Table 2). Second, we quantified the changes in spatial variability at different spatial scales compared to the original 1km resolution by calculating the ratio of σ_{scale} to $\sigma_{1\,km}$. Third, we fitted a $\log\left(\frac{\sigma_{scale}}{\sigma_{1\,\mathrm{km}}}\right) \propto \beta \times \log\left(\frac{\lambda_{scale}}{\lambda_{1\,\mathrm{km}}}\right)$ relationship, where β is an indicator to quantify data spatial variability persistence across scales

(Hu et al., 1997). A more negative β indicates a larger dependency of data spatial variability on spatial scales, resulting in a higher information loss, denoted as $\gamma = (1 - \sigma_{scale}/\sigma_{1\,\mathrm{km}}) \times 100\%$. Given the possibility that β may not demonstrate significant temporal variation (Mälicke et al., 2020), and considering that our scaling analysis is intended for demonstration purposes, our spatial scaling analysis is based on the annual mean of ELM2 simulations.

Table 2. Spatial resolution and pixel number at different spatial scales.

λ_{scale}	1	2	3	4	5	6	12
Spatial resolution	1km (1/120°)	2km (1/60°)	3km (1/40°)	4km (1/30°)	5km (1/24°)	6km (1/20°)	12km (1/10°)
Pixel number within 0.5° × 0.5° box	60 × 60	30 × 30	20 × 20	15 × 15	12 × 12	10 × 10	5 × 5

3.3 Attribution analysis utilizing XML methods

We conducted additional analysis to determine the primary land surface parameters that influence the spatial scaling of ELM simulations. We employed XML methods, specifically the eXtreme Gradient Boosting(XGBoost; Chen and Guestrin, 2016) machine learning algorithm and the game theoretic approach SHapley Additive exPlanations (SHAP; Lundberg and Lee, 2017; Lundberg et al., 2018, 2020). XML methods were utilized to assess the influence of land surface parameters on the spatial variability and information loss of ELM2 simulations across the CONUS. Taking spatial variability as an example, we first computed the standard deviation (σ) within each 0.5º x 0.5º grid for both 1 km resolution land surface parameters and simulations. Then, we train a machine learning model to predict the spatial variability of each simulated variable (i.e., SM, LH, ELR, ASR). We used the spatial variability (i.e., σ) and mean (μ) of the land surface parameters and μ of precipitation and temperature as predictor variables, and the simulated variable's σ as the target variable. After training the machine learning model, we used SHAP to quantify the relative importance and determine which factors were most important in driving the spatial variability of

the simulations. Similarly, we used this approach to identify the most critical drivers of information loss.

3. Results

3.1 Demonstration of the global 1km land surface parameters

LAI generally shows high values in humid and warm regions, such as tropical rainforests, southeastern US, and southern Asia, and low values over arid or cold regions, such as central Australia, southwestern US, Middle East, Central Asia, and northern Canada (Figure 1a). At high resolution, the LAI dataset clearly reflects the detailed heterogeneity of vegetation distributions. In subregion R1 (Figure 1b), a relatively small LAI is distributed over mountain ridges and zero LAI over water surfaces (e.g., lakes). In subregion R2 (Figure 1c), the LAI pattern shows a large proportion of forest fragmentation caused by deforestation. In subregion R3 (Figure 1d), the LAI shows the distribution of agricultural land along with the river, river mouth, and lakes under an arid climate. R4 shows how urbanization affects vegetation distributions (Figure 1e).

Figure 2 demonstrates the distribution of plant functional types and other non-vegetation land units. High-resolution LULC types over multiple years can benefit studies related to LULC changes like urbanization and deforestation. Canopy height generally follows a similar spatial pattern with LAI, with high values in humid and warm regions and low values over arid or cold regions (Figure 3a). The percent clay shows high values over Southeast Asia, India, central Africa, and southeast South America, and low content over North Europe, South Africa and Alaska (Figure 3b). The topography factors follow the elevation patterns (Figures 3c and 3d), where there are large slopes and standard deviation of elevation over mountainous regions, such as the Rocky Mountains in North America, the Himalayas Mountains in Asia, and Andes Mountains in South America.

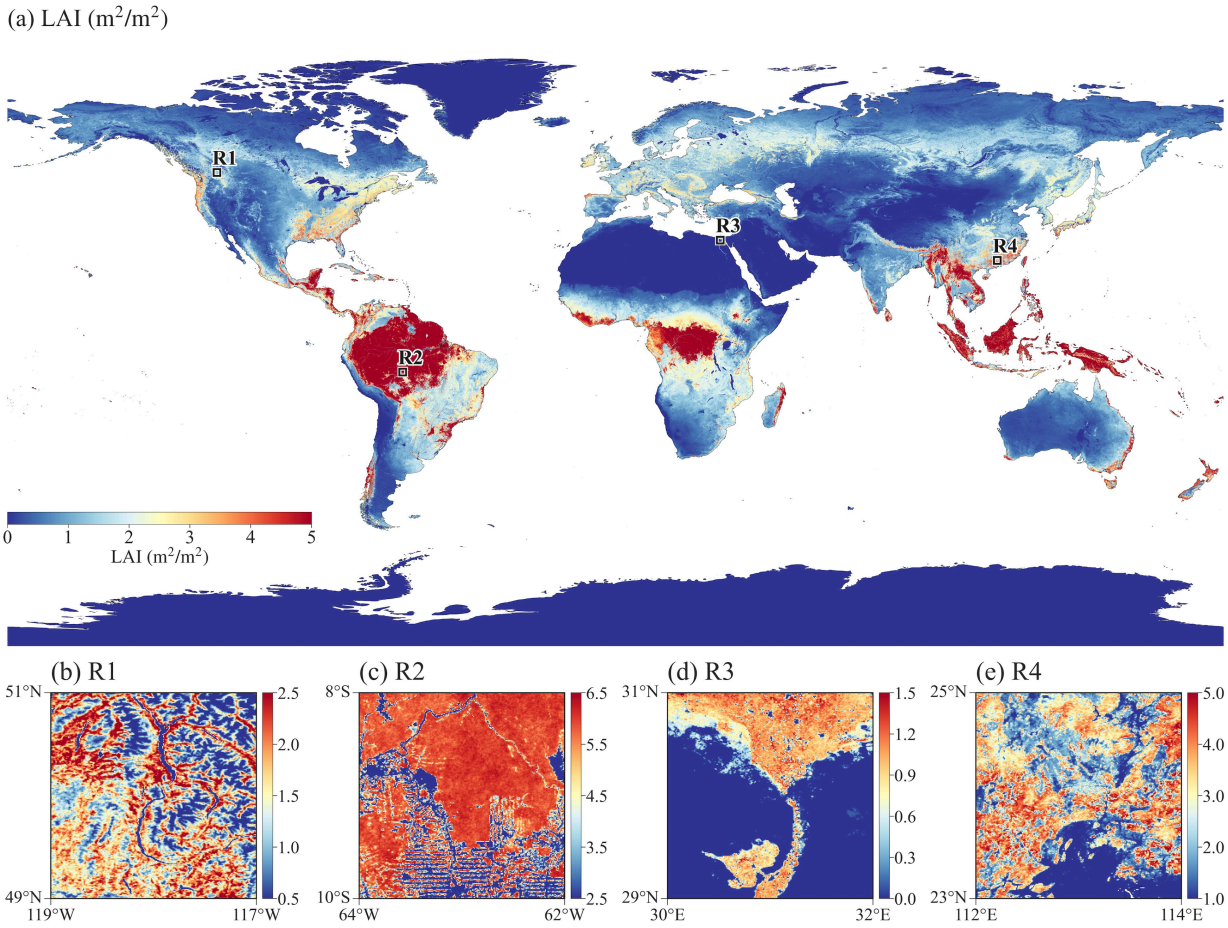

Figure 1. The spatial pattern of LAI (annual mean in 2010) over (a) global land and (b)~(e) four subregions R1~R4 within 2-degree boxes marked in (a).

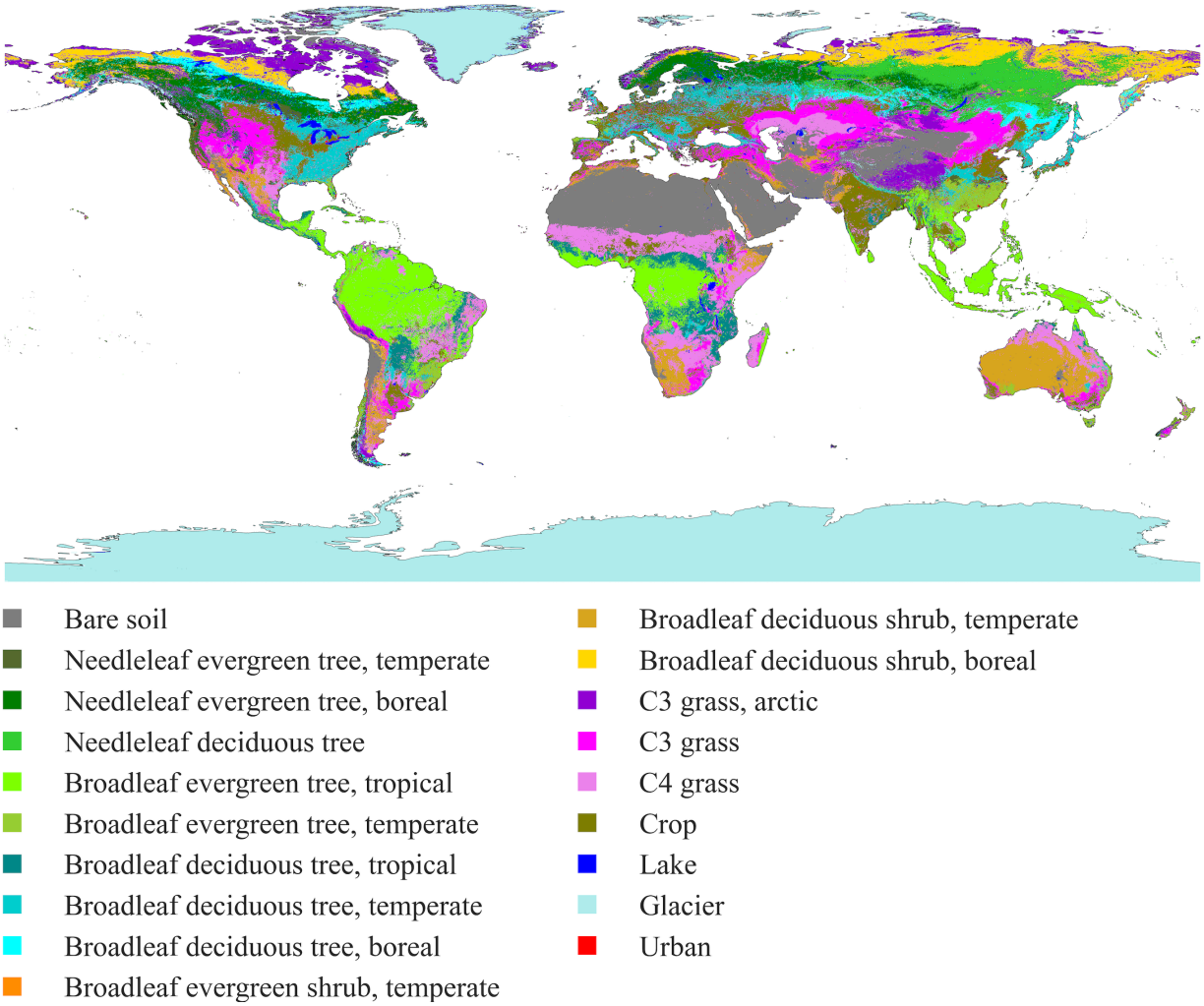

Figure 2. Global LULC distribution in year 2010.

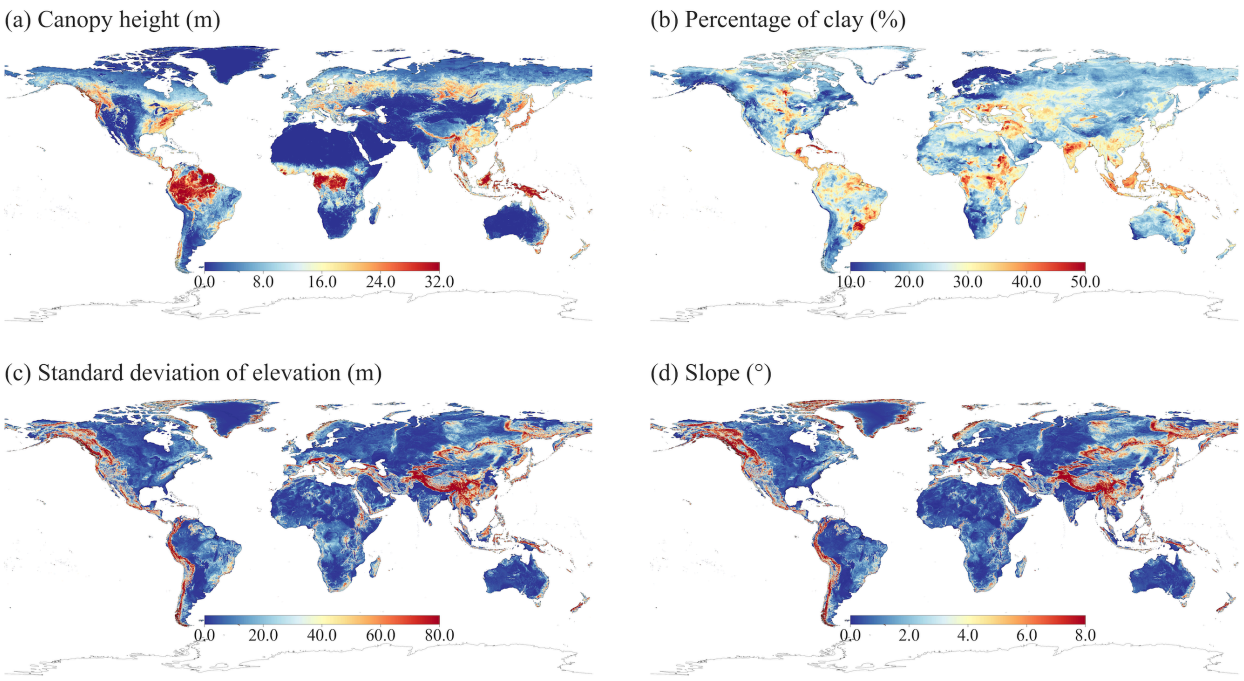

Figure 3. Demonstration of global 1km datasets (a) Canopy top height, (b) percent clay, (c) standard deviation of elevation, and (d) slope.

3.2 Demonstration 1km simulation over CONUS

ELM simulations at a 1 km resolution display significant spatial heterogeneity over CONUS (Figure 4). The values of SM, LH, ELR, and ASR across CONUS follow approximately normal distributions, with averages of 0.3 m^3/m^3, 39.0 W/m^2, 371.7 W/m^2, 156.7 W/m^2, respectively (as shown in the histogram plots in Figure 4). SM shows drier conditions over the West and Southwest and wetter conditions over the Midwest, Corn Belt, Mississippi River basin, and Northeast (Figure 4a). LH shows high values over the central and southeast, and lower values over the west and southwest (Figure 4b). The ELR generally shows higher values over regions with high surface temperature in the south (Figure 4c). The ASR shows higher values over the southwestern regions determined by incoming solar radiation and albedo (Figure 4d). Despite the high-resolution heterogeneity shown at 1 km resolution, we can still see the spatial patterns distinguished at coarse

resolution, i.e., 0.5º × 0.5º. These coarser footprints are from the GSWP3 atmospheric forcing with 0.5º resolution. As concluded by Li et al. (2022), atmospheric forcing is one primary heterogeneity source for land surface modeling. Therefore, k-scale atmospheric forcing needs to be developed to further advance k-scale offline land surface modeling.

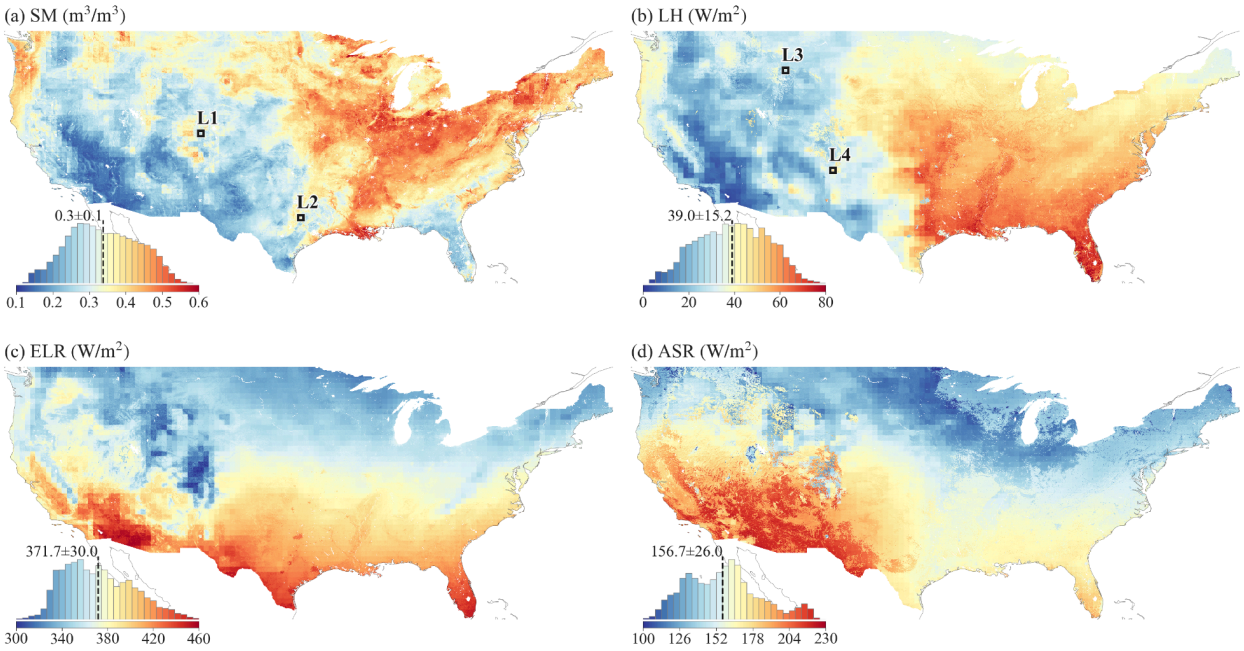

Figure 4. The annual mean of 1 km simulations of (a)SM, (b)LH, (c) ELR, and (ASR) over CONUS. The 0.5° × 0.5° boxes marked as L1, L2, L3, and L4 in (a) and (b) are selected to demonstrate the spatial scaling analysis. The inserted histogram plot illustrates the distribution of ELM2 simulations.

3.3 Demonstration of spatial scaling across scales

We next demonstrate the relationships between spatial variabilities and spatial scales for SM and LH. Four locations (in Figures 4a and 4b) are specifically chosen to showcase varying levels of spatial information loss: L1 and L3 demonstrate a relatively large loss for SM and LH, respectively, while L2 and L4 represent a relatively small loss for SM and LH, respectively.

At location L1 (Figure 5a), when the 1 km simulation is upscaled to coarser resolutions (i.e., larger spatial scale ratios), the spatial variability of SM decreases, resulting in a negative slope of β. As shown in Figure 6a, compared to the original 1 km resolution, the information loss γ reaches up to 54.9% at the 12 km spatial scale. The spatial pattern of SM is consistent with the spatial pattern of percent clay (Figures 6a vs. 6b and 6c vs. 6d), indicating that soil texture contributes significantly to the spatial variability of SM. However, SM has a more negative β than the percent clay (β = –0.28 vs. –0.19 at L1, as shown in Figure 5a), suggesting that SM variability is amplified likely by other processes that are also influenced by soil texture. In contrast to location L1, location L2 exhibits less negative β values for both SM and percent clay, suggesting that their spatial variabilities exhibit less scale dependence (Figures 5a, 6c, and 6d). Both SM and percent clay at location L2 approximately maintain their spatial patterns of high values in the west and low values in the east across spatial scales (Figures 6c and 6d).

For LH, there is a more negative β value at location L3 than at location L4 (β = –0.27 at L3 vs. –0.08 at L4, as shown in Figure 5b), which indicates a larger decrease of spatial variability across spatial scales and lower variability persistence at location L3 than location L4 (Figure 7). The spatial pattern of LH is consistent with the spatial pattern of LAI (Figures 7a vs. 7b and 7c vs. 7d) at different spatial scales, suggesting that vegetation plays a significant role in the spatial variability of LH. Similar to comparison between SM and soil texture, LH has a more negative β than LAI (Figure 5b).

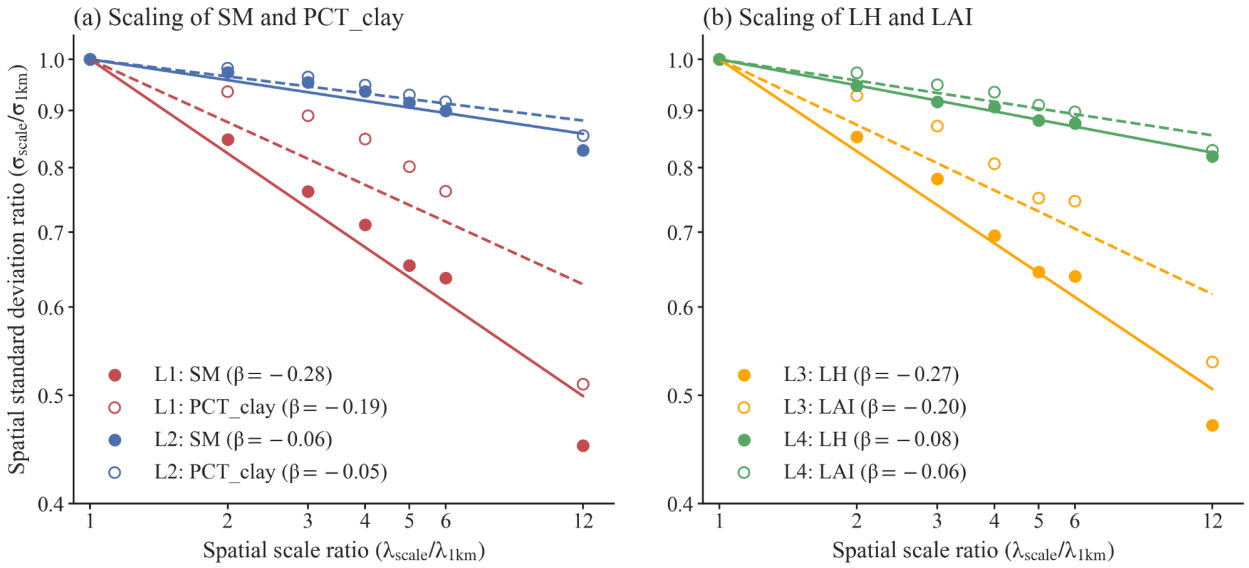

Figure 5. The scaling of spatial variabilities for (a) SM and percent clay, and (b) LH and LAI. Both the x-axis and y-axis are in logarithmic scale. The slope of the linear regression line, β, quantifies the strength of the negative relationship between spatial scale and spatial variability. A more negative β value indicates a higher spatial-scale dependency and increased information loss at coarser spatial scales. Four 0.5° × 0.5° boxes (displayed in Figure 4), namely L1 to L4, are chosen to contrast larger and smaller negative β values for SM and percent clay (L1 and L2) and for LH and LAI (L3 and L4).

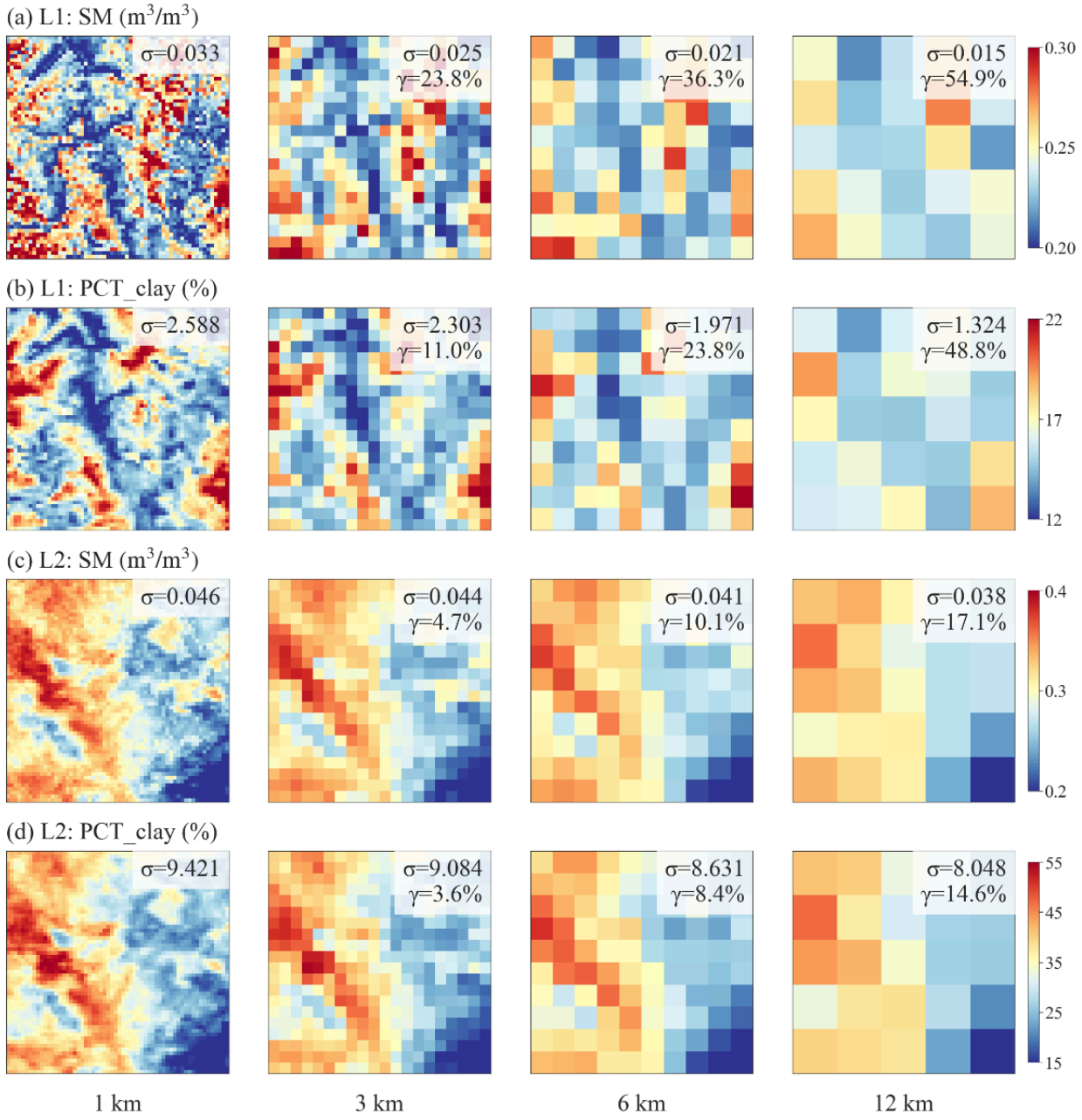

Figure 6. Comparison of SM and percent clay across spatial scales at locations L1 and L2 highlighted in Figure 5. Each subplot displays the spatial patterns of SM or percent clay within a 0.5° × 0.5° box, with the σ and γ presented in the legend.

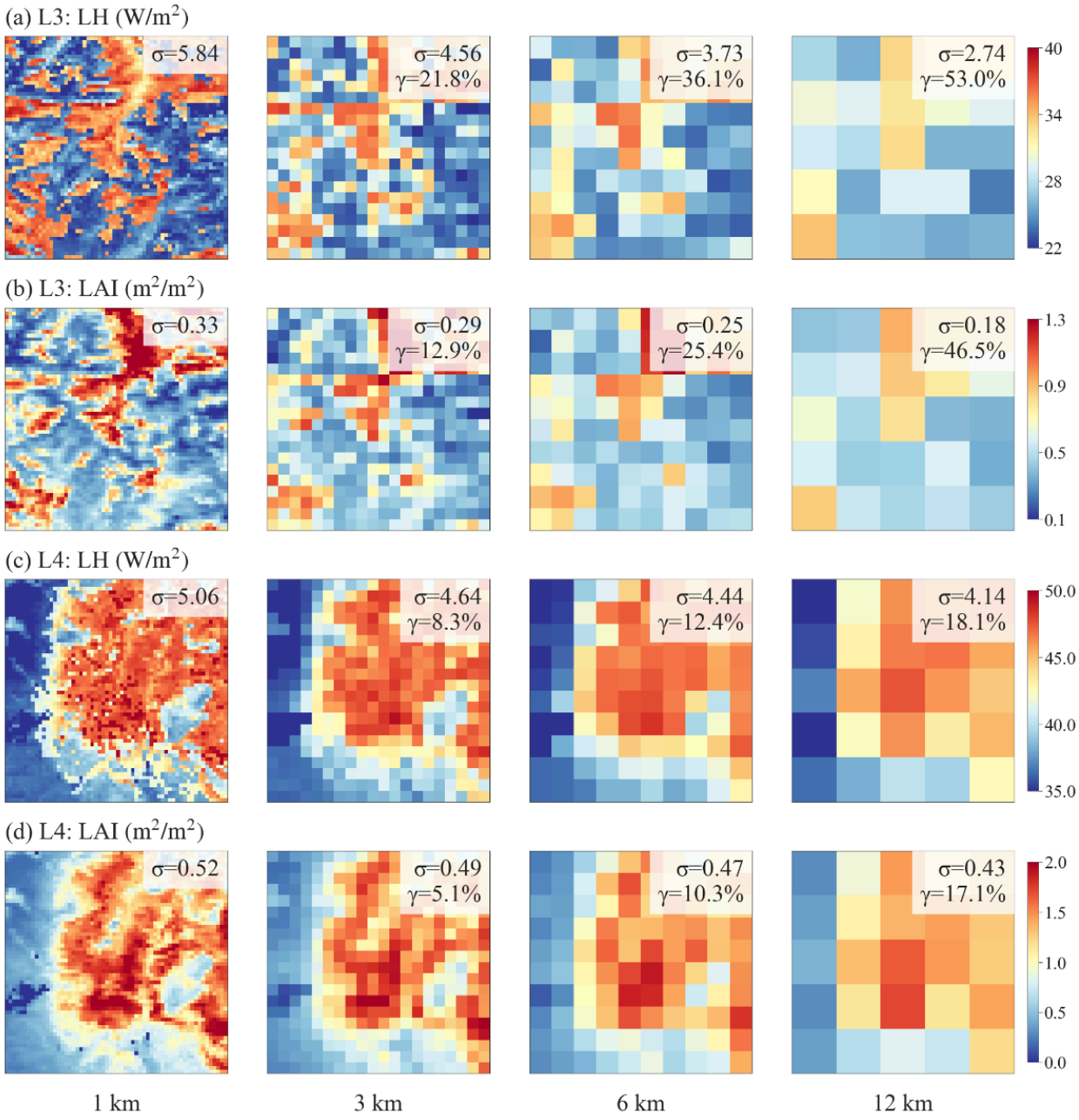

Figure 7. Similar to Figure 6, but for LH and LAI at locations L3 and L4.

3.4 The spatial variability of water and energy simulations and their drivers

We quantified the spatial variability simulated at 1 km resolution using σ within each 0.5º × 0.5º box across CONUS. Four ML models were built to explore the spatial relationships between σ and its potential drivers including σ of the land surface parameters and the temperature and precipitation averaged over the grid box. Overall, the ML models performed well in predicting the σ of the simulated variables, with small root mean square error (RMSE) and large R^2 (see Figure S1). SM shows larger spatial variability in the US Southern Coastal Plain, lower Mississippi River, Northeast, Southeast, and regions around the Great Lake (Figure 8a), which is roughly consistent with the spatial heterogeneity of the high-resolution SM simulation in Vergopolan et al. (2022). Based on the SHAP method, the spatial variability of SM across CONUS is driven by various factors, mainly including the spatial variabilities of percent sand and percent clay, mean precipitation, the σ and μ of soil organic matter, the σ of canopy height, and mean temperature (Figure 8b). Mean precipitation and temperature reflect climate conditions (Figure S3), which are related to the water supply and water demand of soil water content. The spatial heterogeneity of soil properties, such as texture and organic matter content, affects soil hydraulic properties and generate more spatially variable soil water content. Vegetation characteristics, such as canopy height and LAI, could influence SM spatial variability through their effect on roughness length and rooting depth.

The spatial variability of LH is large in the southeastern, central, and western mountainous regions of the US (Figure 8c). Vegetation properties and climate conditions mainly drive the variability of LH (Figure 8d). The μ and σ of LAI can affect transpiration and soil evaporation, while canopy height can influence surface roughness length and, in turn, evapotranspiration. Mean precipitation

and temperature reflect the overall climate conditions related to the water and energy available for latent heat.

ELR and ASR exhibit large spatial variability mainly over the western US, with ASR additionally showing significant spatial variability across the Northern US (Figures 8e and 8g). This variability is primarily driven by climate conditions such as mean precipitation and temperature, topographic features such as standard deviation of elevation and slope, and vegetation properties including LAI and canopy height (Figures 8f and 8h). These factors are related to the radiation input and surface properties, such as albedo and roughness length, which impact the energy cycles and availability of ELR and ASR.

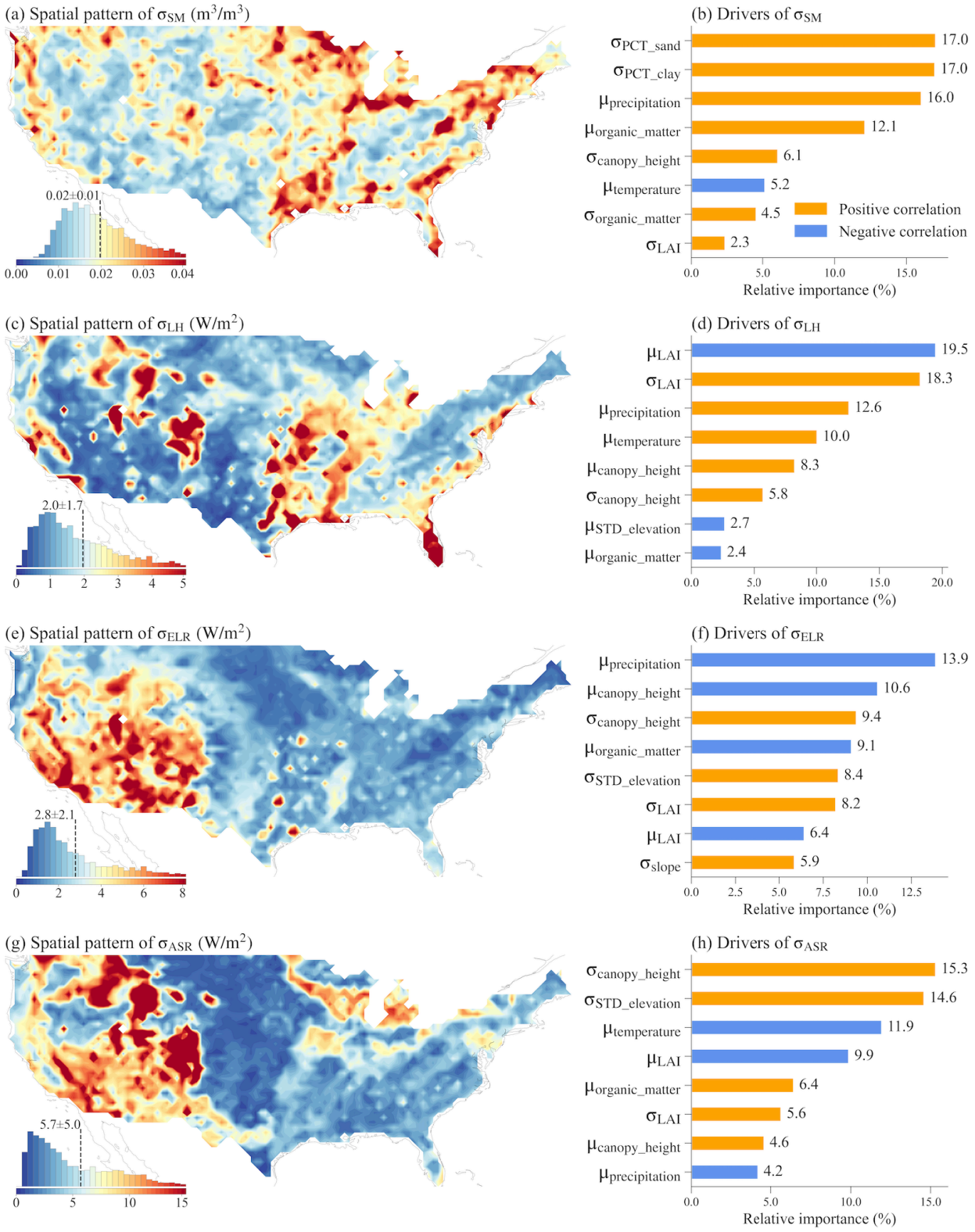

Figure 8. The spatial variability over each 0.5º × 0.5º grid cell (left plots) and the top eight most important drivers (right plots) of the spatial variability for SM, LH, ELR, and ASR. The inserted

histogram plot illustrates the probability distribution of the spatial variability across CONUS. The relative importance of each variable in determining the spatial variability is calculated as the ratio of the mean |SHAP value| of the variable to the sum of the mean |SHAP value| of all variables. Therefore, the sum of the relative importance of all variables is 100%.

3.5 The information loss of water and energy simulations and their drivers

We also evaluated the information loss in simulations when upscaling from 1 km to 12 km resolution and analyzed the drivers of their spatial patterns over CONUS. Four ML models were built to explore the relationships between the γ of the simulations and its drivers including the γ of the land surface parameters and the mean temperature and precipitation averaged over the 0.5º × 0.5º box. These ML models performed well in predicting the simulations' γ, with small RMSE and large R^2 (Figure S2).

Significant information loss ranging from 31% to 54% with maximum values exceeding 90% is observed for SM, LH, ELR, and ASR simulations (Figure 9). Their spatial patterns and drivers show distinct variations. γ_{SM} is primarily driven by the information loss of percent clay and sand, mean soil organic matter, and mean temperature, which affects the soil hydraulic properties and soil water balance (Figures 9a and 9b). γ_{LH} displays high values in the eastern US and low values in the western US (Figure 9c). It is primarily contributed by the information loss of vegetation properties such as LAI and canopy height, and mean LAI, which influences the partitioning of LH and sensible heat, and the partitioning of transpiration and evaporation (Figure 9d). γ_{ELR} exhibits high values in the central and eastern US, particularly in the northeastern US, while γ_{ASR} has high values almost all over the US, especially in the eastern regions (Figures 9e and 9g). γ_{ELR} and γ_{ASR} are largely driven by vegetation properties such as LAI and canopy height, which are associated

with energy processes such as albedo (Figures 9f and 9h). Additionally, topography factors of standard deviation of elevation and slope also slightly contribute to γ_{ASR}.

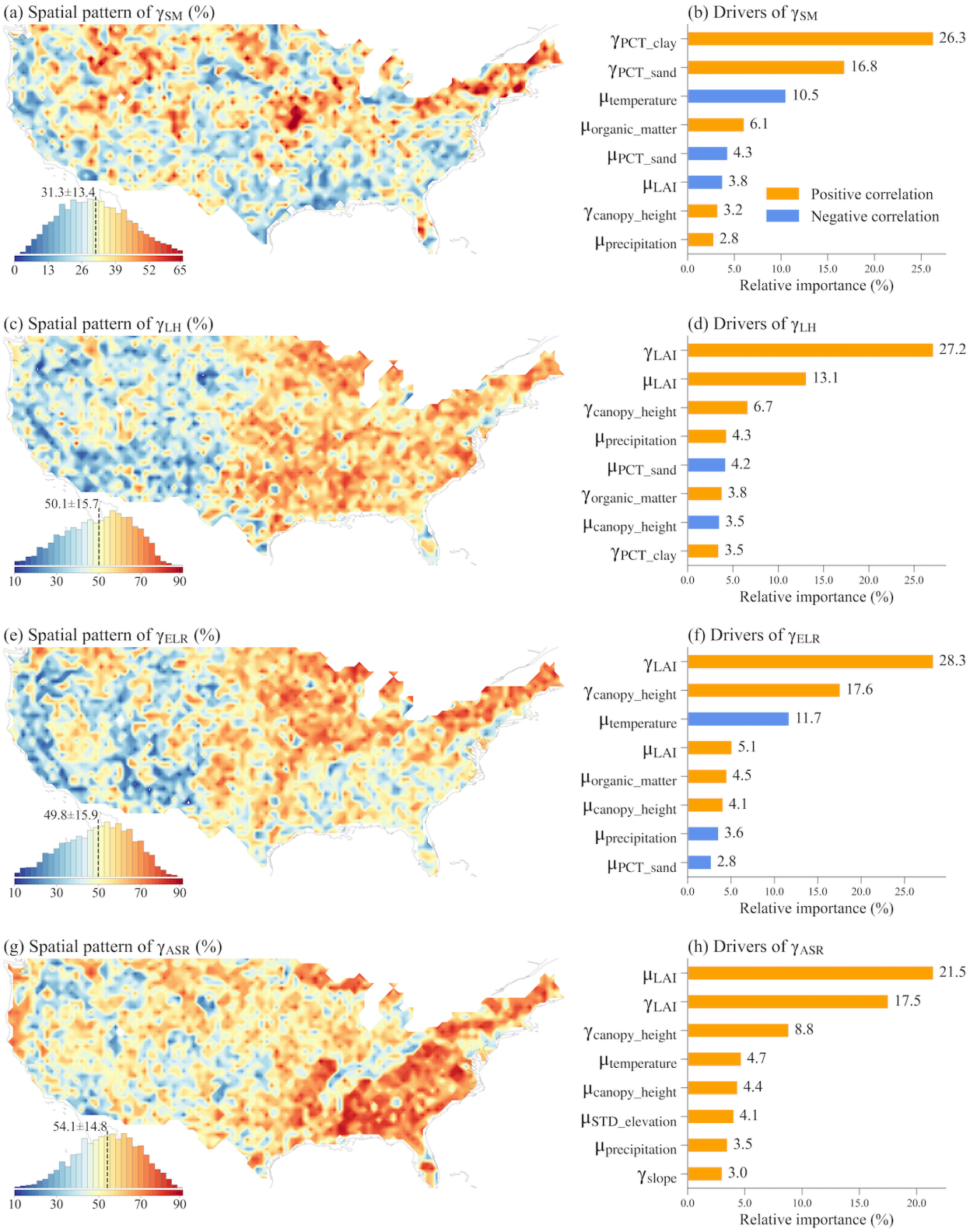

Figure 9. Same as Figure 8 but for information loss.

4. Discussion

The new 1 km land surface parameter datasets developed in this study represent significant improvements over the current datasets. Compared to the two common land surface parameter datasets of CLM5 and K2012, our data are more advanced by utilizing the newest high-resolution data sources, including MODIS PFTs and non-vegetation land units, LAI and SAI, canopy height, soil properties and topography factors. The availability of multi-year data for LULC, LAI, and SAI parameters is advantageous for studies such as LULC changes, including urbanization, deforestation, and agricultural impacts. Incorporating these new 1 km land surface parameters into ESMs will advance the accurate representation and understanding of land surface processes and land–atmosphere interactions. However, certain limitations and opportunities for future development should be noted. The urban extension may differ depending on the data sources, urban definitions, and the algorithms employed, such as those derived from harmonized nighttime lights (Zhao et al., 2022), global artificial impervious area (GAIA, Li et al., 2020b; Gong et al., 2020), urban expansion (Liu et al., 2020; Kuang et al., 2021), which may differ from our urban land units based on MODIS. The urban classification into TBD, HD, and MD in J2010 is based on the global building height. Although there are building height datasets available for specific regions, such as Europe, the US, and China (Yang and Zhao, 2022; Li et al., 2020a; Frantz et al., 2021; Cao and Huang, 2021) , a globally consistent building height dataset is currently not publicly accessible, which hinders the future improvement of urban classification. The multiple-year high-resolution PFT maps developed by the European Space Agency's Climate Change Initiative could be used to further extend this dataset for a longer period (Harper et al., 2023).

The new 1 km land surface parameters can improve k-scale offline LSMs modeling by better capturing spatial surface heterogeneity. As evidenced by the 1 km ELM simulation over CONUS, soil properties, vegetation properties, and topographic factors contribute to the spatial heterogeneities of ELM water and energy simulations. Upscaling 1 km to a coarser 12 km resolution, we observe significant spatial information loss, with SM experiencing an average loss of 31%, and LH, ELR, and ASR experiencing around 50% information loss on average. This conclusion is in line with the results of Vergopolan et al. (2022), which showed a substantial loss of spatial information in soil moisture when upscaling from 30 m to 1 km resolution, with an average loss of approximately 48% and up to 80% over the CONUS region. The XML analysis reveals that the spatial variability and information loss of ELM2 simulations are influenced by the spatial variability and information loss of the different variables of land surface parameters, as well as the mean precipitation and temperature. Our findings highlight the critical role of land surface parameters in contributing to the spatial variability of water and energy in land surface simulations, showcasing the value of the developed high-resolution datasets. Another implementation example where our 1 km land surface parameters can be beneficial is in hillslope-scale simulations, which are fundamental for organizing water, energy, and biogeochemical processes (Fan et al., 2019). Krakauer et al. (2014) have highlighted the significance of between-cell groundwater flow, which becomes comparable in magnitude to recharge at grid spacings smaller than 10 km. Advancements have been made in ESMs to address hillslope-scale processes, including the representation of intra-hillslope lateral subsurface flow within grid cells in CLM5 (Swenson et al., 2019), the development of explicit lateral flow processes between grid cells (Qiu et al., 2023), and the incorporation of topographic radiation effects within and between grid cells (Hao et al., 2021). Another notable example is the integrated hydrology-land surface model ParFlow-CLM, which incorporates three-

dimensional groundwater flow, two-dimensional overland flow, and land surface exchange processes (Maxwell, 2013). ParFlow-CLM has demonstrated remarkable reliability in reproducing hydrologic processes, such as its simulations at 3 km resolution for pan-European and 1 km resolution for CONUS (Naz et al., 2023; O'Neill et al., 2021). More recently, Fang et al. (2022) coupled ParFlow with ELM and the Functionally Assembled Terrestrial Ecosystem Simulator (FATES) to simulate carbon-hydrology interactions at hillslope scale. By incorporating our 1 km datasets and leveraging these advancements, we can improve simulations of hillslope-scale processes and enhance our understanding of water and energy dynamics within ESMs.

The new land surface parameters are also a timely resource for supporting the emerging need for k-scale Earth system modeling. Representing the impact of spatial heterogeneity on land-atmosphere interaction processes is a major challenge in Earth system modeling. Taking E3SM as an example, researchers have proposed three key approaches to enhance spatial heterogeneity representation to address this challenge. In line with these approaches, our newly developed 1 km land surface parameters offer promising opportunities for improving land-atmosphere coupling within ESMs. The first approach to enhance the representation of spatial heterogeneity is to directly conduct simulations at high resolution. For instance, the Simple Cloud-Resolving E3SM Atmosphere Model (SCREAM) has been used to perform global simulations at 3.25 km (Caldwell et al., 2021), although the land surface parameters were based on coarser resolution datasets. By utilizing the new 1 km land surface parameters, we can enhance the representation of land surface heterogeneity within the ELM component of SCREAM, potentially improving modeling of land–atmosphere coupling. The second and third approaches focus on improving the representation of land surface heterogeneity within ESMs run at a coarse resolution while accounting for subgrid

heterogeneity in two different ways. In the second approach, the Cloud Layers Unified By Binormals (CLUBB) has been implemented in E3SM Atmosphere Model (EAM) version 1 (Rasch et al., 2019; Bogenschutz et al., 2013), to better account for subgrid atmospheric heterogeneity of turbulent mixing, shallow convection, and cloud macrophysics. Recently, Huang et al. (2022) developed a novel land-atmosphere coupling scheme in EAM that enables the communication of subgrid land surface heterogeneity information to the atmosphere model with CLUBB, significantly impacting boundary layer dynamics. The new 1km datasets can provide more accurate land surface representations of the variability of individual patches and the inter-patch variability that were used in Huang et al. (2022). The third approach is the Multiple Atmosphere Multiple Land (MAML) approach used in the multiscale modeling framework (MMF) in which a cloud resolving model (CRM) is embedded within each grid cell of the atmosphere (Baker et al., 2019; Lin et al., 2023; Lee et al., 2023). In the MAML approach, each CRM column within the atmosphere grid is coupled directly with its own independent land surface. This enables a more explicit representation of the impact of spatial heterogeneity on land-atmosphere interactions within each grid and has shown notable impacts on water and energy simulations (Baker et al., 2019; Lin et al., 2023). Lee et al. (2023) highlighted the limitation of the current MAML approach, which utilizes the same land surface characteristics for each land surface model interacting with the CRM column within the same grid, which could lead to a weak representation of land-atmosphere interactions. To address this limitation, incorporating the new 1 km land surface parameters within the MAML approach can provide more detailed information about land surface heterogeneity, enabling a more accurate capture of land-atmosphere interactions.

5. Data availability

The 1 km land surface parameters are publicly available at https://doi.org/10.25584/PNNLDH/1986308 (Li et al., 2023).

6. Conclusion

We developed 1 km global land surface parameters using the latest available datasets covering multiple years from 2001 to 2020. These parameters comprise four categories: LULC of PFTs and non-vegetative land cover, vegetation properties, soil properties, and topographic factors. The 1 km resolution ELM simulations conducted over CONUS demonstrate the valuable capabilities of the new datasets in enabling k-scale land surface modeling. Through scaling analysis of the 1 km resolution simulations within 0.5º × 0.5º boxes where spatial heterogeneity of the simulations is induced only by spatial heterogeneity of the land surface parameters, we revealed the significant impact of land surface parameters on the spatial variability of water and energy simulations. The spatial information loss of these simulations over CONUS is significant when upscaling from 1 km to a coarser 12 km resolution, with an average ranging from 31% to 54% and up to more than 90%. The XML analysis reveals that the spatial variability and spatial information loss of ELM2 simulations are primarily impacted by the spatial variability and information loss of soil properties, vegetation properties and topography factors, as well as the mean climate conditions of precipitation and temperature. Furthermore, the spatial variability of water and energy in the 1 km simulations is not dominated by the spatial heterogeneity of any land surface parameters, suggesting the usefulness of the multi-parameter high-resolution land surface parameter dataset. The availability of 1 km land surface parameters is a valuable resource that addresses the emerging needs of k-scale LSMs and ESMs modeling. By providing accurate and precise information, these

1 km land surface parameters will significantly enhance our understanding of the water, carbon, and energy cycles under global change.

Author contributions

LL, GB, and DH designed the study, processed the datasets, conducted experiments, and drafted the manuscript. LRL contributed to the conceptual design, discussion of results, and manuscript revisions.

Acknowledgments

This study is supported by the US Department of Energy (DOE) Office of Science Biological and Environmental Research as part of the Regional and Global Model Analysis (RGMA) program area through the collaborative, multi-program Integrated Coastal Modeling (ICoM) project. This study used DOE's Biological and Environmental Research Earth System Modeling program's Compy computing cluster at Pacific Northwest National Laboratory. We thank Ye Liu at PNNL for providing suggestions on processing the canopy height dataset. Pacific Northwest National Laboratory is operated for the US Department of Energy by Battelle Memorial Institute under contract DE-AC05-76RL01830. DH acknowledges the support from the US DOE, Office of Science, Office of Biological and Environmental Research, Earth System Model Development program area, as part of the Climate Process Team projects.

Financial support

This work was supported by the Regional and Global Modeling and Analysis program area of the US Department of Energy, Office of Science, Office of Biological and Environmental Research, as part of the multi-program, collaborative integrated Coastal Modeling (ICoM) project (grant no. KP1703110/75415).

Competing interests

At least one of the (co-)authors is a member of the editorial board of the Earth System Science Data. The authors have no other competing interests to declare.

Reference

Arendt, A., Bliss , A., Bolch, T., et al.: Randolph Glacier Inventory–A Dataset of Global Glacier Outlines Version: 1.0, Global Land Ice Measurements from Space, Boulder Colorado, USA. Digital Media, 2012.

Baker, I. T., Denning, A. S., Dazlich, D. A., Harper, A. B., Branson, M. D., Randall, D. A., Phillips, M. C., Haynes, K. D., and Gallup, S. M.: Surface-Atmosphere Coupling Scale, the Fate of Water, and Ecophysiological Function in a Brazilian Forest, J Adv Model Earth Sy, 11, 2523–2546, https://doi.org/10.1029/2019ms001650, 2019.

Batjes, N.H.: ISRIC-WISE derived soil properties on a 5 by 5 arc-minutes global grid. Report 2006/02, available through : http://www.isric.org, 2006.

Bogenschutz, P. A., Gettelman, A., Morrison, H., Larson, V. E., Craig, C., and Schanen, D. P.: Higher-Order Turbulence Closure and Its Impact on Climate Simulations in the Community Atmosphere Model, J Climate, 26, 9655–9676, https://doi.org/10.1175/jcli-d-13-00075.1, 2013.

Bonan, G. B., Oleson, K. W., Vertenstein, M., Levis, S., Zeng, X., Dai, Y., Dickinson, R. E., and Yang, Z.-L.: The Land Surface Climatology of the Community Land Model Coupled to the NCAR Community Climate Model*, J Climate, 15, 3123–3149, https://doi.org/10.1175/1520-0442(2002)015<;3123:tlscot>2.0.co;2, 2002.

Bonan, G. B., Levis, S., Kergoat, L., & Oleson, K. W.: Landscapes as patches of plant functional types: An integrating concept for climate and ecosystem models. Global Biogeochemical Cycles, 16(2), 5-1–5-23. https://doi.org/10.1029/2000gb001360, 2002

Bou-Zeid, E., Anderson, W., Katul, G. G., and Mahrt, L.: The Persistent Challenge of Surface Heterogeneity in Boundary-Layer Meteorology: A Review, Bound-lay Meteorol, 177, 227–245, https://doi.org/10.1007/s10546-020-00551-8, 2020.

Caldwell, P. M., Mametjanov, A., Tang, Q., Roekel, L. P. V., Golaz, J., Lin, W., Bader, D. C., Keen, N. D., Feng, Y., Jacob, R., Maltrud, M. E., Roberts, A. F., et al.: The DOE E3SM Coupled Model Version 1: Description and Results at High Resolution, J Adv Model Earth Sy, 11, 4095–4146, https://doi.org/10.1029/2019ms001870, 2019.

Caldwell, P. M., Terai, C. R., Hillman, B., Keen, N. D., Bogenschutz, P., Lin, W., et al.: Convection-Permitting Simulations With the E3SM Global Atmosphere Model, J Adv Model Earth Sy, 13, https://doi.org/10.1029/2021ms002544, 2021.

Cao, Y. and Huang, X.: A deep learning method for building height estimation using high-resolution multi-view imagery over urban areas: A case study of 42 Chinese cities, Remote Sens Environ, 264, 112590, https://doi.org/10.1016/j.rse.2021.112590, 2021.

Chaney, N. W., Huijgevoort, M. H. J. V., Shevliakova, E., Malyshev, S., Milly, P. C. D., Gauthier, P. P. G., and Sulman, B. N.: Harnessing big data to rethink land heterogeneity in Earth

system models, Hydrol Earth Syst Sc, 22, 3311–3330, https://doi.org/10.5194/hess-22-3311-2018, 2018.

Change, N. C.: Think big and model small, Nat Clim Change, 12, 493–493, https://doi.org/10.1038/s41558-022-01399-1, 2022.

Chen, J., Hagos, S., Xiao, H., Fast, J. D., and Feng, Z.: Characterization of Surface Heterogeneity-Induced Convection Using Cluster Analysis, J Geophys Res Atmospheres, 125, https://doi.org/10.1029/2020jd032550, 2020.

Chen, T. and Guestrin, C.: XGBoost: A Scalable Tree Boosting System, Proc 22nd Acm Sigkdd Int Conf Knowl Discov Data Min, 785–794, https://doi.org/10.1145/2939672.2939785, 2016.

Defries, R. S., Hansen, M. C., Townshend, J. R. G., Janetos, A. C., and Loveland, T. R.: A new global 1-km dataset of percentage tree cover derived from remote sensing: GLOBAL PERCENTAGE TREE COVER FROM REMOTE SENSING, Global Change Biol, 6, 247–254, https://doi.org/10.1046/j.1365-2486.2000.00296.x, 2000.

Dozier, J.: Revisiting Topographic Horizons in the Era of Big Data and Parallel Computing, Ieee Geosci Remote S, 19, 1–5, https://doi.org/10.1109/lgrs.2021.3125278, 2022.

Fan, Y., Clark, M., Lawrence, D. M., Swenson, S., Band, L. E., Brantley, S. L., et al.: Hillslope Hydrology in Global Change Research and Earth System Modeling, Water Resour Res, 55, 1737–1772, https://doi.org/10.1029/2018wr023903, 2019.

Frantz, D., Schug, F., Okujeni, A., Navacchi, C., Wagner, W., Linden, S. van der, and Hostert, P.: National-scale mapping of building height using Sentinel-1 and Sentinel-2 time series, Remote Sens Environ, 252, 112128, https://doi.org/10.1016/j.rse.2020.112128, 2021.

Friedl, M. A., McIver, D. K., Hodges, J. C. F., Zhang, X. Y., Muchoney, D., Strahler, A. H., Woodcock, C. E., Gopal, S., Schneider, A., Cooper, A., Baccini, A., Gao, F., and Schaaf, C.: Global land cover mapping from MODIS: algorithms and early results, Remote Sens Environ, 83, 287–302, https://doi.org/10.1016/s0034-4257(02)00078-0, 2002.

Friedl, M. A., Sulla-Menashe, D., Tan, B., Schneider, A., Ramankutty, N., Sibley, A., and Huang, X.: MODIS Collection 5 global land cover: Algorithm refinements and characterization of new datasets, Remote Sens Environ, 114, 168–182, https://doi.org/10.1016/j.rse.2009.08.016, 2010.

Friedl, M., Sulla-Menashe, D.: MCD12Q1 MODIS/Terra+Aqua Land Cover Type Yearly L3 Global 500m SIN Grid V006 [Data set]. NASA EOSDIS Land Processes DAAC. Accessed 2022-11-21 from https://doi.org/10.5067/MODIS/MCD12Q1.006, 2019.

Giorgi, F. and Avissar, R.: Representation of heterogeneity effects in Earth system modeling: Experience from land surface modeling, Rev Geophys, 35, 413–437, https://doi.org/10.1029/97rg01754, 1997.

Gorelick, N., Hancher, M., Dixon, M., Ilyushchenko, S., Thau, D., & Moore, R.: Google Earth Engine: Planetary-scale geospatial analysis for everyone. Remote Sensing of Environment, 202, 18–27. https://doi.org/10.1016/j.rse.2017.06.031, 2017.

Gong, P., Li, X., Wang, J., Bai, Y., Chen, B., Hu, T., Liu, X., Xu, B., Yang, J., Zhang, W., and Zhou, Y.: Annual maps of global artificial impervious area (GAIA) between 1985 and 2018, Remote Sens Environ, 236, 111510, https://doi.org/10.1016/j.rse.2019.111510, 2020.

Gorelick, N., Hancher, M., Dixon, M., Ilyushchenko, S., Thau, D., and Moore, R.: Google Earth Engine: Planetary-scale geospatial analysis for everyone, Remote Sens Environ, 202, 18–27, https://doi.org/10.1016/j.rse.2017.06.031, 2017.

Hansen, M. C., DeFries, R. S., Townshend, J. R. G., Carroll, M., Dimiceli, C., and Sohlberg, R. A.: Global Percent Tree Cover at a Spatial Resolution of 500 Meters: First Results of the MODIS Vegetation Continuous Fields Algorithm, Earth Interact, 7, 1–15, https://doi.org/10.1175/1087-3562(2003)007<;0001:gptcaa>2.0.co;2, 2003.

Hao, D., Bisht, G., Huang, M., Ma, P., Tesfa, T., Lee, W., Gu, Y., and Leung, L. R.: Impacts of Sub-Grid Topographic Representations on Surface Energy Balance and Boundary Conditions in the E3SM Land Model: A Case Study in Sierra Nevada, J Adv Model Earth Sy, 14, https://doi.org/10.1029/2021ms002862, 2022.

Harper, K. L., Lamarche, C., Hartley, A., Peylin, P., Ottlé, C., Bastrikov, V., Martín, R. S., Bohnenstengel, S. I., Kirches, G., Boettcher, M., Shevchuk, R., Brockmann, C., and Defourny, P.: A 29-year time series of annual 300 m resolution plant-functional-type maps for climate models, Earth Syst Sci Data, 15, 1465–1499, https://doi.org/10.5194/essd-15-1465-2023, 2023.

Hengl, T., Jesus, J. M. de, Heuvelink, G. B. M., Gonzalez, M. R., Kilibarda, M., Blagotić, A., Shangguan, W., Wright, M. N., et al.: SoilGrids250m: Global gridded soil information based on machine learning, Plos One, 12, e0169748, https://doi.org/10.1371/journal.pone.0169748, 2017.

Hewitt, H., Fox-Kemper, B., Pearson, B., Roberts, M., and Klocke, D.: The small scales of the ocean may hold the key to surprises, Nat Clim Change, 12, 496–499, https://doi.org/10.1038/s41558-022-01386-6, 2022.

Hijmans, R. J., Cameron, S. E., Parra, J. L., Jones, P. G., and Jarvis, A.: Very high resolution interpolated climate surfaces for global land areas, International Journal of Climatology, 25, 1965–1978, https://doi.org/10.1002/joc.1276, 2005.

Hu, Z., Islam, S., and Cheng, Y.: Statistical characterization of remotely sensed soil moisture images, Remote Sens Environ, 61, 310–318, https://doi.org/10.1016/s0034-4257(97)89498-9, 1997.

Huang, M., Ma, P.-L., Chaney, N. W., Hao, D., Bisht, G., Fowler, M. D., Larson, V. E., and Leung, L. R.: Representing surface heterogeneity in land-atmosphere coupling in E3SMv1

single-column model over ARM SGP during summertime, Geoscientific Model Dev Discuss, 2022, 1–20, https://doi.org/10.5194/gmd-2021-421, 2022.

Hugelius, G., Tarnocai, C., Broll, G., Canadell, J. G., Kuhry, P., and Swanson, D. K.: The Northern Circumpolar Soil Carbon Database: spatially distributed datasets of soil coverage and soil carbon storage in the northern permafrost regions, Earth Syst. Sci. Data, 5, 3–13, https://doi.org/10.5194/essd-5-3-2013, 2013.

IGBP: Global Soil Data Task (IGBP-DIS, ISO-image of CD). International Geosphere-Biosphere Program, PANGAEA, https://doi.org/10.1594/PANGAEA.869912, 2000.

Jackson, T. L., Feddema, J. J., Oleson, K. W., Bonan, G. B., and Bauer, J. T.: Parameterization of Urban Characteristics for Global Climate Modeling, Ann Assoc Am Geogr, 100, 848–865, https://doi.org/10.1080/00045608.2010.497328, 2010.

Jarvis, A., H.I. Reuter, A. Nelson, E. Guevara.: Hole-filled SRTM for the globe Version 4, available from the CGIAR-CSI SRTM 90m Database: https://srtm.csi.cgiar.org, 2008.

Ji, P. and Yuan, X.: High-Resolution Land Surface Modeling of Hydrological Changes Over the Sanjiangyuan Region in the Eastern Tibetan Plateau: 2. Impact of Climate and Land Cover Change, J Adv Model Earth Sy, 10, 2829–2843, https://doi.org/10.1029/2018ms001413, 2018.

Ji, P., Yuan, X., Shi, C., Jiang, L., Wang, G., and Yang, K.: A Long-Term Simulation of Land Surface Conditions at High Resolution over Continental China, J Hydrometeorol, 24, 285–314, https://doi.org/10.1175/jhm-d-22-0135.1, 2023.

Ke, Y., Leung, L. R., Huang, M., Coleman, A. M., Li, H., and Wigmosta, M. S.: Development of high resolution land surface parameters for the Community Land Model, Geosci Model Dev, 5, 1341–1362, https://doi.org/10.5194/gmd-5-1341-2012, 2012.

Ke, Y., Leung, L. R., Huang, M., and Li, H.: Enhancing the representation of subgrid land surface characteristics in land surface models, Geosci Model Dev, 6, 1609–1622, https://doi.org/10.5194/gmd-6-1609-2013, 2013.

Kim, H.: Global Soil Wetness Project Phase 3 Atmospheric Boundary Conditions (Experiment 1) [Data set]. Data Integration and Analysis System (DIAS). https://doi.org/10.20783/DIAS.501, 2017.

Kourzeneva, E.: Global dataset for the parameterization of lakes in Numerical Weather Prediction and Climate modeling. ALADIN Newsletter, No 37, July-December, 2009, F. Bouttier and C. Fischer, Eds., Meteo-France, Toulouse, France, 46-53, 2009.

Kourzeneva, E.: External data for lake parameterization in Numerical Weather Prediction and climate modeling. Boreal Environment Research, 15, 165-177, 2010.

Krakauer, N. Y., Li, H., and Fan, Y.: Groundwater flow across spatial scales: importance for climate modeling, Environ Res Lett, 9, 034003, https://doi.org/10.1088/1748-9326/9/3/034003, 2014.

Kuang, W., Du, G., Lu, D., Dou, Y., Li, X., Zhang, S., Chi, W., Dong, J., Chen, G., Yin, Z., Pan, T., Hamdi, R., Hou, Y., Chen, C., Li, H., and Miao, C.: Global observation of urban expansion and land-cover dynamics using satellite big-data, Sci Bull, 66, 297–300, https://doi.org/10.1016/j.scib.2020.10.022, 2021.

Lang, N., Jetz, W., Schindler, K., and Wegner, J. D.: A high-resolution canopy height model of the Earth, Arxiv, https://doi.org/10.48550/arxiv.2204.08322, 2022.

Lawrence, D. M., Fisher, R. A., Koven, C. D., Oleson, K. W., Swenson, S. C., Bonan, G., et al.: The Community Land Model Version 5: Description of New Features, Benchmarking, and Impact of Forcing Uncertainty, J Adv Model Earth Sy, 11, 4245–4287, https://doi.org/10.1029/2018ms001583, 2019.

Lawrence, D., Fisher, R., Koven, C., Oleson, K., Swenson, S., et al. (2018). Technical description of version 5.0 of the Community Land Model (CLM). National Center for Atmospheric Research, University Corporation for Atmospheric Research, Boulder, CO. https://escomp.github.io/ctsm-docs/versions/release-clm5.0/html/tech_note/index.html

Lee, J., Hannah, W. M., and Bader, D. C.: Representation of atmosphere induced heterogeneity in land – atmosphere interactions in E3SM-MMFv2, Geoscientific Model Dev Discuss, 2023, 1–21, https://doi.org/10.5194/gmd-2023-55, 2023.

Leng, G., Huang, M., Tang, Q., Sacks, W. J., Lei, H., and Leung, L. R.: Modeling the effects of irrigation on land surface fluxes and states over the conterminous United States: Sensitivity to input data and model parameters, J Geophys Res Atmospheres, 118, 9789–9803, https://doi.org/10.1002/jgrd.50792, 2013.

Leung, L. R., Bader, D. C., Taylor, M. A., and McCoy, R. B.: An Introduction to the E3SM Special Collection: Goals, Science Drivers, Development, and Analysis, J Adv Model Earth Sy, 12, https://doi.org/10.1029/2019ms001821, 2020.

Li, L., Bisht, G., and Leung, L. R.: Spatial heterogeneity effects on land surface modeling of water and energy partitioning, Geosci Model Dev, 15, 5489–5510, https://doi.org/10.5194/gmd-15-5489-2022, 2022.

Li, X., Zhou, Y., Gong, P., Seto, K. C., and Clinton, N.: Developing a method to estimate building height from Sentinel-1 data, Remote Sens Environ, 240, 111705, https://doi.org/10.1016/j.rse.2020.111705, 2020a.

Li, X., Gong, P., Zhou, Y., Wang, J., Bai, Y., Chen, B., Hu, T., Xiao, Y., et al.: Mapping global urban boundaries from the global artificial impervious area (GAIA) data, Environ Res Lett, 15, 094044, https://doi.org/10.1088/1748-9326/ab9be3, 2020b.

Li, L., Bisht, G., Hao, D., Leung, L.R.: Global 1km Land Surface Parameters for Kilometer Scale Earth System Modeling, Pacific Northwest National Laboratory DataHub [data set], https://doi.org/10.25584/PNNLDH/1986308, 2023.

Lin, G., Leung, L. R., Lee, J., Harrop, B. E., Baker, I. T., Branson, M. D., Denning, A. S., Jones, C. R., Ovchinnikov, M., Randall, D. A., and Yang, Z.: Modeling Land-Atmosphere Coupling at Cloud-Resolving Scale Within the Multiple Atmosphere Multiple Land (MAML) Framework in SP-E3SM, J Adv Model Earth Sy, 15, https://doi.org/10.1029/2022ms003101, 2023.

Liu, S., Shao, Y., Kunoth, A., and Simmer, C.: Impact of surface-heterogeneity on atmosphere and land-surface interactions, Environ Modell Softw, 88, 35–47, https://doi.org/10.1016/j.envsoft.2016.11.006, 2017.

Liu, X., Huang, Y., Xu, X., Li, X., Li, X., Ciais, P., Lin, P., et al.: High-spatiotemporal-resolution mapping of global urban change from 1985 to 2015, Nat Sustain, 3, 564–570, https://doi.org/10.1038/s41893-020-0521-x, 2020.

Lundberg, S. and Lee, S.-I.: A Unified Approach to Interpreting Model Predictions, Arxiv, 2017.

Lundberg, S. M., Nair, B., Vavilala, M. S., Horibe, M., Eisses, M. J., Adams, T., Liston, D. E., Low, D. K.-W., Newman, S.-F., Kim, J., and Lee, S.-I.: Explainable machine-learning predictions for the prevention of hypoxaemia during surgery, Nat Biomed Eng, 2, 749–760, https://doi.org/10.1038/s41551-018-0304-0, 2018.

Lundberg, S. M., Erion, G., Chen, H., DeGrave, A., Prutkin, J. M., Nair, B., Katz, R., Himmelfarb, J., Bansal, N., and Lee, S.-I.: From local explanations to global understanding with explainable AI for trees, Nat Mach Intell, 2, 56–67, https://doi.org/10.1038/s42256-019-0138-9, 2020.

Mälicke, M., Hassler, S. K., Blume, T., Weiler, M., and Zehe, E.: Soil moisture: variable in space but redundant in time, Hydrol Earth Syst Sc, 24, 2633–2653, https://doi.org/10.5194/hess-24-2633-2020, 2020.

Maxwell, R. M.: A terrain-following grid transform and preconditioner for parallel, large-scale, integrated hydrologic modeling, Adv Water Resour, 53, 109–117, https://doi.org/10.1016/j.advwatres.2012.10.001, 2013.

Myneni, R. B., Hoffman, S., Knyazikhin, Y., Privette, J. L., Glassy, J., Tian, Y., Wang, Y., Song, X., Zhang, Y., Smith, G. R., Lotsch, A., Friedl, M., Morisette, J. T., Votava, P., Nemani, R. R., and Running, S. W.: Global products of vegetation leaf area and fraction absorbed PAR from year one of MODIS data, Remote Sens Environ, 83, 214–231, https://doi.org/10.1016/s0034-4257(02)00074-3, 2002.

Myneni, R., Knyazikhin, Y., Park, T. (2021). MODIS/Terra+Aqua Leaf Area Index/FPAR 4-Day L4 Global 500m SIN Grid V061 [Data set]. NASA EOSDIS Land Processes DAAC. Accessed 2022-11-21 from https://doi.org/10.5067/MODIS/MCD15A3H.061

Naz, B. S., Sharples, W., Ma, Y., Goergen, K., and Kollet, S.: Continental-scale evaluation of a fully distributed coupled land surface and groundwater model, ParFlow-CLM (v3.6.0), over Europe, Geosci Model Dev, 16, 1617–1639, https://doi.org/10.5194/gmd-16-1617-2023, 2023.

Nitta, T., Arakawa, T., Hatono, M., Takeshima, A., & Yoshimura, K: Development of integrated land simulator, Prog Earth Planet Sci, 7(1), 1-14, https://doi.org/10.1186/s40645-020-00383-7, 2020.

O'Neill, M. M. F., Tijerina, D. T., Condon, L. E., and Maxwell, R. M.: Assessment of the ParFlow–CLM CONUS 1.0 integrated hydrologic model: evaluation of hyper-resolution water balance components across the contiguous United States, Geosci Model Dev, 14, 7223–7254, https://doi.org/10.5194/gmd-14-7223-2021, 2021.

Poggio, L., Sousa, L. M. de, Batjes, N. H., Heuvelink, G. B. M., Kempen, B., Ribeiro, E., and Rossiter, D.: SoilGrids 2.0: producing soil information for the globe with quantified spatial uncertainty, Soil, 7, 217–240, https://doi.org/10.5194/soil-7-217-2021, 2021.

Qiu, H., Bisht, G., Li, L., Hao, D., and Xu, D.: Development of Inter-Grid Cell Lateral Unsaturated and Saturated Flow Model in the E3SM Land Model (v2.0), Egusphere, 2023, 1–31, https://doi.org/10.5194/egusphere-2023-375, 2023.

Rabus, B., Eineder, M., Roth, A., & Bamler, R.: The shuttle radar topography mission—A new class of digital elevation models acquired by spaceborne radar. ISPRS Journal of Photogrammetry and Remote Sensing, 57(4), 241–262. https://doi.org/10.1016/s0924-2716(02)00124-7, 2003.

Ramankutty, N. and Foley, J. A.: Estimating historical changes in global land cover: Croplands from 1700 to 1992, Global Biogeochem Cy, 13, 997–1027, https://doi.org/10.1029/1999gb900046, 1999.

Rasch, P. J., Xie, S., Ma, P. -L., Lin, W., Wang, H., Tang, Q., Burrows, S. M., Caldwell, P., et al.: An Overview of the Atmospheric Component of the Energy Exascale Earth System Model, J Adv Model Earth Sy, 11, 2377–2411, https://doi.org/10.1029/2019ms001629, 2019.

Rastner, P., Bolch, T., Mölg, N., Machguth, H., Le Bris, R., and Paul, F.: The first complete inventory of the local glaciers and ice caps on Greenland, The Cryosphere, 6, 1483–1495, https://doi.org/10.5194/tc-6-1483-2012, 2012.

Rouf, T., Maggioni, V., Mei, Y., and Houser, P.: Towards hyper-resolution land-surface modeling of surface and root zone soil moisture, J Hydrol, 594, 125945, https://doi.org/10.1016/j.jhydrol.2020.125945, 2021.

Simard, M., Pinto, N., Fisher, J. B., and Baccini, A.: Mapping forest canopy height globally with spaceborne lidar, Journal of Geophysical Research: Biogeosciences, 116, G04021, https://doi.org/10.1029/2011jg001708, 2011.

Singh, R. S., Reager, J. T., Miller, N. L., and Famiglietti, J. S.: Toward hyper-resolution land-surface modeling: The effects of fine-scale topography and soil texture on CLM4.0 simulations over the Southwestern U.S., Water Resour Res, 51, 2648–2667, https://doi.org/10.1002/2014wr015686, 2015.

Slingo, J., Bates, P., Bauer, P., Belcher, S., Palmer, T., Stephens, G., Stevens, B., Stocker, T., and Teutsch, G.: Ambitious partnership needed for reliable climate prediction, Nat Clim Change, 12, 499–503, https://doi.org/10.1038/s41558-022-01384-8, 2022.

Still, C. J., Berry, J. A., Collatz, G. J., and DeFries, R. S.: Global distribution of C3 and C4 vegetation: Carbon cycle implications, Global Biogeochem Cy, 17, 6-1-6–14, https://doi.org/10.1029/2001gb001807, 2003.

Sulla-Menashe, D., Gray, J. M., Abercrombie, S. P., and Friedl, M. A.: Hierarchical mapping of annual global land cover 2001 to present: The MODIS Collection 6 Land Cover product, Remote Sens Environ, 222, 183–194, https://doi.org/10.1016/j.rse.2018.12.013, 2019.

Swenson, S. C., Clark, M., Fan, Y., Lawrence, D. M., and Perket, J.: Representing Intrahillslope Lateral Subsurface Flow in the Community Land Model, J Adv Model Earth Sy, 11, 4044–4065, https://doi.org/10.1029/2019ms001833, 2019.

Verdin, K. L. and Greenlee, S. K.: Development of continental scale digital elevation models and extraction of hydrographic features, paper presented at the Third International Workshop on Integrating GIS and Environmental Modeling, Santa Fe, New Mexico, 21–26 January, Natl. Cent. for Geogr. Inf. and Anal., Santa Barbara, Calif, 1996.

Vergopolan, N., Chaney, N. W., Beck, H. E., Pan, M., Sheffield, J., Chan, S., and Wood, E. F.: Combining hyper-resolution land surface modeling with SMAP brightness temperatures to obtain 30-m soil moisture estimates, Remote Sens Environ, 242, 111740, https://doi.org/10.1016/j.rse.2020.111740, 2020.

Vergopolan, N., Chaney, N. W., Pan, M., Sheffield, J., Beck, H. E., Ferguson, C. R., Torres-Rojas, L., Sadri, S., and Wood, E. F.: SMAP-HydroBlocks, a 30-m satellite-based soil moisture dataset for the conterminous US, Sci Data, 8, 264, https://doi.org/10.1038/s41597-021-01050-2, 2021.

Vergopolan, N., Sheffield, J., Chaney, N. W., Pan, M., Beck, H. E., Ferguson, C. R., Torres-Rojas, L., Eigenbrod, F., Crow, W., and Wood, E. F.: High-Resolution Soil Moisture Data Reveal Complex Multi-Scale Spatial Variability Across the United States, Geophys Res Lett, 49, https://doi.org/10.1029/2022gl098586, 2022.

Vrese, P. de, Schulz, J.-P., and Hagemann, S.: On the Representation of Heterogeneity in Land-Surface–Atmosphere Coupling, Bound-lay Meteorol, 160, 157–183, https://doi.org/10.1007/s10546-016-0133-1, 2016.

Wood, E. F., Roundy, J. K., Troy, T. J., Beek, L. P. H. van, Bierkens, M. F. P., et al.: Hyperresolution global land surface modeling: Meeting a grand challenge for monitoring Earth's terrestrial water, Water Resour Res, 47, https://doi.org/10.1029/2010wr010090, 2011.

Xia, Y., Mocko, D., Huang, M., Li, B., Rodell, M., Mitchell, K. E., Cai, X., and Ek, M. B.: Comparison and Assessment of Three Advanced Land Surface Models in Simulating Terrestrial Water Storage Components over the United States, J Hydrometeorol, 18, 625–649, https://doi.org/10.1175/jhm-d-16-0112.1, 2017.

Yamazaki, D., Ikeshima, D., Sosa, J., Bates, P. D., Allen, G. H., and Pavelsky, T. M.: MERIT Hydro: A High-Resolution Global Hydrography Map Based on Latest Topography Dataset, Water Resour Res, 55, 5053–5073, https://doi.org/10.1029/2019wr024873, 2019.

Yang, C. and Zhao, S.: A building height dataset across China in 2017 estimated by the spatially-informed approach, Sci Data, 9, 76, https://doi.org/10.1038/s41597-022-01192-x, 2022.

Yuan, H., Dai, Y., Xiao, Z., Ji, D., and Shangguan, W.: Reprocessing the MODIS Leaf Area Index products for land surface and climate modelling, Remote Sens Environ, 115, 1171–1187, https://doi.org/10.1016/j.rse.2011.01.001, 2011.

Yuan, X., Ji, P., Wang, L., Liang, X., Yang, K., Ye, A., Su, Z., and Wen, J.: High-Resolution Land Surface Modeling of Hydrological Changes Over the Sanjiangyuan Region in the Eastern Tibetan Plateau: 1. Model Development and Evaluation, J Adv Model Earth Sy, 10, 2806–2828, https://doi.org/10.1029/2018ms001412, 2018.

Zeng, X., Shaikh, M., Dai, Y., Dickinson, R. E., and Myneni, R.: Coupling of the Common Land Model to the NCAR Community Climate Model, J Climate, 15, 1832–1854, https://doi.org/10.1175/1520-0442(2002)015<;1832:cotclm>2.0.co;2, 2002.

Zhao, M., Cheng, C., Zhou, Y., Li, X., Shen, S., and Song, C.: A global dataset of annual urban extents (1992–2020) from harmonized nighttime lights, Earth Syst Sci Data, 14, 517–534, https://doi.org/10.5194/essd-14-517-2022, 2022.

Zhou, Y., Li, D., and Li, X.: The Effects of Surface Heterogeneity Scale on the Flux Imbalance under Free Convection, J Geophys Res Atmospheres, 124, 8424–8448, https://doi.org/10.1029/2018jd029550, 2019.